Beam speed effects on Ti–6Al–4V microstructures in electron beam additive manufacturing

Xibing Gong
Department of Mechanical Engineering, The University of Alabama, Tuscaloosa, Alabama 35487, USA
James Lydon and Kenneth Cooper
Advanced Manufacturing Technology Team, Marshall Space Flight Center, Huntsville, Alabama 35812, USA
Kevin Chou[a)]
Department of Mechanical Engineering, The University of Alabama, Tuscaloosa, Alabama 35487, USA

(Received 28 February 2014; accepted 2 June 2014)

The effect of the beam scanning speed on part microstructures in the powder-bed electron beam additive manufacturing (EBAM) process was investigated in this research. Four levels of the beam speed were tested in building EBAM Ti–6Al–4V samples. The samples were subsequently used to prepare metallographic specimens for observations by optical microscopy and scanning electron microscopy. During the experiment, a near-infrared thermal imager was also used to acquire build surface temperatures for melt tool size estimates. It was found that the X-plane (side surface) shows columnar prior β grains, with the width in the range of about 40–110 μm, and martensitic structures. The width of columnar grains decreases with the increase of the scanning speed. In addition, the Z-plane (scanning surface) shows equiaxed grains, in the range of 50–85 μm. The grain size from the lowest beam speed (214 mm/s) is much larger compared to other samples of higher beam speeds (e.g., 376–689 mm/s). In addition, increasing the beam scanning speed will also result in finer α-lath. However, the porosity defect on the build surface also becomes severe at the highest scanning speed (689 mm/s).

I. INTRODUCTION

Additive manufacturing (AM), a layer-based manufacturing process, has emerged as a promising fabrication technology embraced by different industries for numerous applications. Powder-bed electron beam additive manufacturing (EBAM), using an electron beam to melt and fuse powder, is one of a few AM technologies for direct digital manufacturing of metal products.[1] (There is also a wire-fed EBAM technology, commonly known as electron beam freeform fabrication (EBF[3]). For the sake of simple terminology, EBAM will be used throughout this paper, referring to the powder-bed EBAM process.) Because of several unique advantages such as a high energy efficiency, a rapid scan speed, and a moderate operation cost, EBAM has attracted ever increasing interest from aerospace, military, and biomedical industries.

Research subjects in EBAM have spread across a wide spectrum ranging from material and microstructural characterization,[1,2] process modeling and simulation,[3–5] process metrology,[6] and to geometric attributes.[7] Even with many potential benefits over conventional manufacturing technologies, EBAM still exhibits several challenges such as part accuracy and property variations. Cooke and Soons[8] studied the geometric accuracy of EBAM parts. It is observed that the dimensional and form errors of EBAM parts are significantly larger than those of typical machined parts.

Ti–6Al–4V is one of the most commonly used alloys in EBAM. Microstructures of Ti–6Al–4V parts produced by EBAM contain a mixture of phases such as α (hexagonal closed packed, HCP), β (body centered cubic, BCC), and α′ martensite (HCP). Columnar-shaped prior β structures formed during initial solidification were observed, which is a result of very high temperature gradients along the build direction.[9,10] Antonysamy et al.[11] studied the prior β grain texture of EBAM components and reported that the columnar structure shows strong fiber textures of <001> β, which is normal to the deposited powder layers. On the other hand, Safdar et al.[10] reported typical Widmanstätten (α + β) inside of prior β grains. Moreover, Facchini et al.[12] investigated Ti–6Al–4V microstructures in EBAM and showed that the main constituent in EBAM-made Ti–6Al–4V is α with only a small fraction of β. In addition, Christensen et al.[13] compared the EBAM microstructures to counterparts from a casting process. For the cast part, a coarse acicular (α + β) and thick prior β grain boundaries can be observed, while the microstructure of the EBAM part consisted of fine acicular (α + β) and thin prior β grain boundaries. The thickness of the α-lath is around 1.4–2.1 μm

[a)]Address all correspondence to this author.
e-mail: kchou@eng.ua.edu
DOI: 10.1557/jmr.2014.125

 © Materials Research Society 2014

https://doi.org/10.1557/jmr.2014.125 Published online by Cambridge University Press

for different EBAM samples.[1] Due to high cooling rates during the solidification, α′-martensitic platelets also exist in EBAM parts, which may contribute to increased strength and hardness, but lower ductility.[14,15] In summary, Ti–6Al–4V parts from EBAM show a fine Widmanstätten (α + β) microstructure combined with α′, which can be expected by the thermal characteristics of the EBAM process, i.e., very rapid cooling.

The microstructures of EBAM Ti–6Al–4V also vary with the process conditions. It has been reported that EBAM process parameters may have significant effects on the part quality.[16,17] Murr et al.[16] reported that variations during the melting stage including the beam current and the scan speed affect EBAM built defects such as porosity, which may be related to the microstructure-property variations in the final product.[18] The electron beam scanning speed is one of the critical parameters in the EBAM process.[3] Jamshidinia et al.[19] applied a finite element model to study heat distributions in EBAM using Ti–6Al–4V powder. It was reported that the cooling rate at 1000 mm/s scanning speed is about 170,800 °C/s, versus about 15,300 °C/s and 1300 °C/s for the beam speed of 500 mm/s and 100 mm/s, respectively. Although various aspects in EBAM were investigated and reported, there has been little systematic study of the relationship between the beam speed and the microstructure of the EBAM parts.

The objective of this experimental study is to better understand the microstructural variations, in terms of phases and characteristic length, affected by the beam scanning speed in Ti–6Al–4V from EBAM. A commercial EBAM system was used to fabricate samples with different beam speeds during the same build cycles for microstructural analysis. Moreover, a thermal imager was applied to acquire process temperatures during the build process. The intent is to correlate part microstructures with process thermal characteristics.

II. EXPERIMENTAL PROCEDURE

An Arcam S12 EBAM machine (Arcam, Sweden) at NASA's Marshall Space Flight Center (Huntsville, AL) was used to fabricate samples, which were simple blocks (60 mm long, 5.5 mm wide, and 25 mm high) modeled from CAD software. Fine pre-alloyed Ti–6Al–4V powder, with a diameter primarily in the range between 45 and 100 μm, was used as feedstock materials; the composition of Ti–6Al–4V powder used is shown in Table I. The layer thickness was 70 μm. The EBAM process involves powder spreading, preheating, as well as contour and hatch melting. During the melting stages, an electron beam moves across the powder-layer surface tracing the cross-section boundary of the part and then raster-scans through the inside of the contour.

TABLE I. Chemical analysis for Ti–6Al–4V powder in wt.%.[2]

Element	Al	V	C	Fe	O	N	H	Ti
EBAM	6	4	0.03	0.1	0.15	0.01	0.003	Bal.
Standard	5.5–6.75	3.5–4.5	<0.1	<0.3	<0.2	<0.05	<0.01	Bal.

Electron beam scanning in an EBAM system is controlled by magnetic deflection coils, which enables very high scanning speeds, e.g., 15 m/s. For Arcam EBAM systems, the speed function (SF) is a process parameter setting related to the actual beam scanning speed.[20] In this study, four different SFs were tested (20, 36, 50, and 65) to investigate the beam speed effects on build part microstructures. Figure 1 shows the EBAM-fabricated samples processed with the corresponding SF. It is noted that the scanning speed affects the surface defects such as porosity. Pores are very prevalent at the final build surface of the sample using SF 65.

A LumaSense MCS640 near-infrared (NIR) camera (LumaSense Technologies, Santa Clara, CA) was used for temperature measurements during the EBAM experiments. The NIR camera has a spectral range of 0.78–1.08 μm and a 640 × 480 pixel uncooled focal plane array sensor. The image capturing system has a maximum frame rate of 60 Hz and a detectable temperature range of 600–3000 °C. The NIR camera was mounted on a tripod and positioned to look downward through the EBAM machine's viewport onto the build platform. The emissivity of Ti–6Al–4V at high temperatures and the liquid state is not known, and thus, the emissivity setting of the NIR camera was assigned as 0.35. The details of the camera setting and setup with the EBAM system can be found in a previous study.[6] For the current study, the acquired thermal images were analyzed to obtain the average temperature profiles around the beam location and to estimate the melt pool sizes for each SF case and at the same build height of 24.43 mm. Moreover, the thermal videos acquired were used to calculate the actual beam speed values during the melting stage, by evaluating the molten pool movement between consecutive frames. It was found that the beam speed is related to both the SF and the

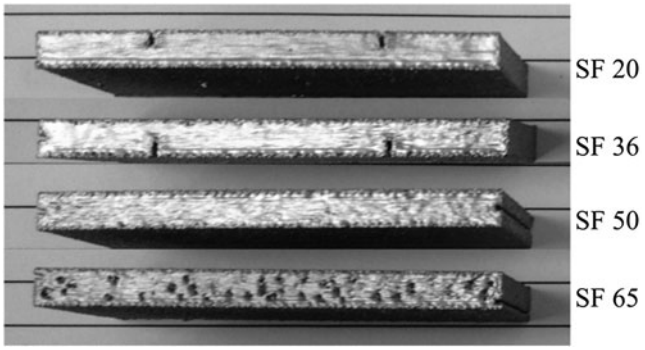


FIG. 1. EBAM parts built with different SFs.

https://doi.org/10.1557/jmr.2014.125 Published online by Cambridge University Press

build height, using the relationships found, a regression equation for the beam speed is shown in Eq. (1).

$$v = (-0.7343h + 28.554)\mathrm{SF} \quad , \qquad (1)$$

where v is the translational beam speed in mm/s, h is the build height in mm, and SF is the speed function index. The beam speeds calculated using the equation were compared to the experimental data and were found to match closely, with a maximum error of 6.6%.

Fabricated Ti–6AL–4V samples were prepared for microstructural observations using standard metallographic procedures including sectioning, mounting, grinding with SiC papers up to the grit size of 1000, and then polished using diamond suspension down to 0.5 μm. Specimens were cut from near the top surface of the build parts for analysis. Specimens of different cross-sections (scanning surface: Z-plane, build side surface: X-plane) were prepared to examine the anisotropic conditions in microstructures. To reveal the microstructures, polished specimens were then etched with a hydrofluoric acid-based solution: 1 mL hydrofluoric acid (50 wt.%) and 3 mL nitric acid (60 wt.%) in 7 mL distilled water.[16] The etched metallographic samples were examined using a Leitz optical microscope (OM; Leitz Microscope, Germany) and a Philips XL-30 scanning electron microscope (SEM; Philips, Netherlands). To quantify the size of columnar β, equiaxed β, and α-lath, a measurement method from the literature (Wang et al.[21]) was applied.

III. RESULTS AND DISCUSSION

A. Typical microstructures

Figure 2 shows a typical microstructure from the X-plane (side surface) of an EBAM sample at SF 36. It is obvious that prior β grains grew along the build direction and across the built-layers in the sample. The solidification of Ti–6Al–4V alloy involves two steps: liquid to primary solid phase of β and solid phase transformation, β to α or α′, depending on the cooling rate. The nucleation and growth of columnar grains of prior β take place during initial rapid solidification before the temperature drops to the β-transus temperature (about 980 °C). The columnar prior β grains are typically associated with high-energy materials processing, and upon rapid cooling from the melt, the growing grains align themselves with the steepest temperature gradients[22] and result in a columnar-shaped morphology.[23] According to the study of Antonysamy et al.,[11] in EBAM, the nucleation of β grains occurred heterogeneously from the boundary layers at the build plate or the part surfaces. The authors also studied the prior β-grain texture of EBAM components and the columnar structure shows strong fiber texture of <001> β along the build direction, which may be attributed to the elongated shape of the moving molten pool.

Another feature in typical EBAM Ti–6Al–4V microstructures is the martensitic phase, α′, which appears as

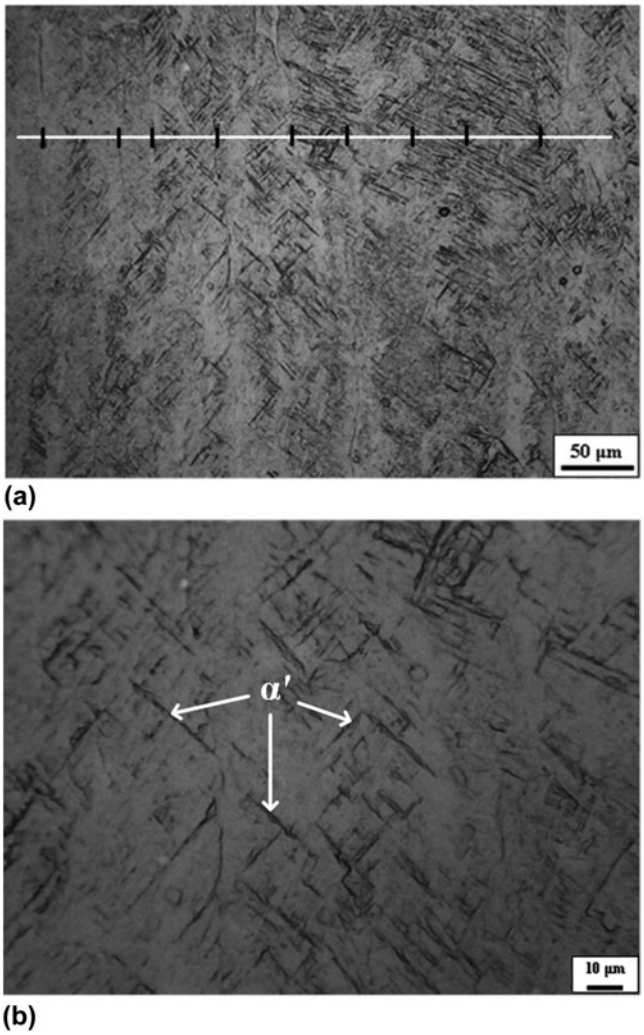


FIG. 2. Microstructure of X-plane (side surface) specimen from an EBAM sample (SF 36): (a) low magnification showing columnar width analysis, and (b) high magnification image.

plates, as can be seen in Fig. 2. The α′ is transformed from the β phase due to a very high cooling rate. According to the study of Ahmed and Rack,[24] for Ti–6Al–4V, a cooling rate of more than 410 °C/s, from the single β to the (α + β) region, will induce α′ formations. In addition, to trigger the formation of martensite, the temperature must be lower than the martensite starting temperature (M_S) of 575 °C.[22] Other researchers, however, reported the M_S as 650 °C and the martensite finishing temperature as 400 °C.[25] The α′ phase is commonly observed in Ti–6Al–4V alloy subject to rapid solidifications such as selective laser melting[26] and electron beam welding.[27]

The width of the columnar prior β grains was measured in this study. Figure 2(a) illustrates an example of the width measurements. The image was overlaid with straight lines which are normal to the boundaries of the columnar structures, and the intersections of the lines with grain boundaries were examined and used for the width estimate.

https://doi.org/10.1557/jmr.2014.125 Published online by Cambridge University Press

Different images from different specimen areas were measured to obtain statistical data. The average width of the columnar structure is about 41.6 μm for this case (SF 36). This result is smaller than the columnar width reported by Al-Bermani et al.,[9] 75–150 μm.

Figures 3 and 4 illustrate a typical microstructure of the Z-plane (scanning surface) specimen, also from the SF 36 sample. Different from the microstructure from the X-plane (Fig. 2), equiaxed grains are noted. Hence, it can be concluded that the prior β grains are of a rod shape. Similar equiaxed grains at the scanning surface have also been reported for Ti–6Al–4V alloy[9] and other alloys[28,29] by other researchers. Figures 3(b) and 4 show higher magnification images of the Z-plane specimen from OM and SEM, respectively; both α and β phases can be identified. Upon cooling from the β-transus temperature, the initial α that nucleates is the so-called "grain boundary" α (α_{GB}) because of its location on a β boundary. Eventually, the β boundaries will be replaced by α_{GB} in a continuous fashion,[22] as can be noted from Fig. 4(a). In addition, fine Widmanstätten (α + β) structures are shown inside of equiaxed grains, indicating a rapid cooling rate in EBAM. Widmanstätten (α + β) is a typical microstructure in Ti–6Al–4V parts produced by EBAM, as can be clearly identified from high magnification images, Figs. 3(b) and 4(b). In solid phase transformation, the prior β columnar grains are transformed into fine α laths. The (α + β) structure is formed by diffusion controlled solid phase transformation, during which V diffuses into β while Al diffuses into α.[10] Further, the classical α-lath structure is surrounded by a very small amount of β in the α boundaries. This result is similar to the studies from Safdar et al.[10] and Murr et al.[14] Compared with the wrought or cast Ti–6Al–4V, EBAM Ti–6Al–4V parts show a finer α phase. Al-Bermani et al.[9] also reported that fine α laths have no preferred texture which is different from strong texturing of prior β grains.

Similar to the measurement method for the columnar width, intersections of the lines with prior β grain boundaries were marked and used for the grain size estimate. The microstructural image was overlaid with

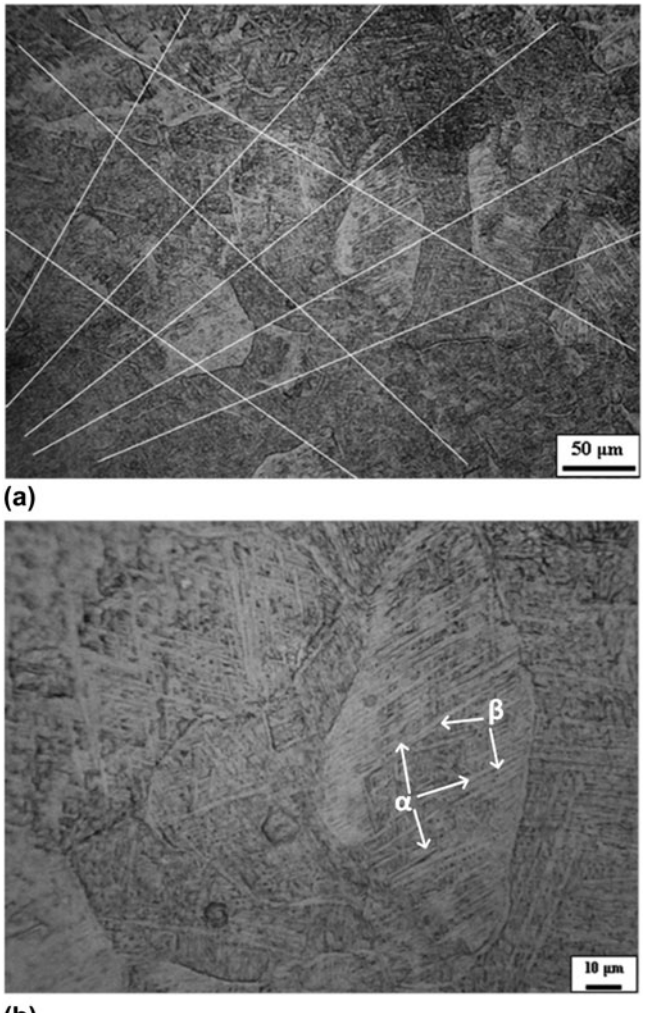


FIG. 3. Microstructure of Z-plane (scanning surface) specimen from an EBAM sample (SF 36): (a) low magnification showing grain size analysis, and (b) high magnification image.

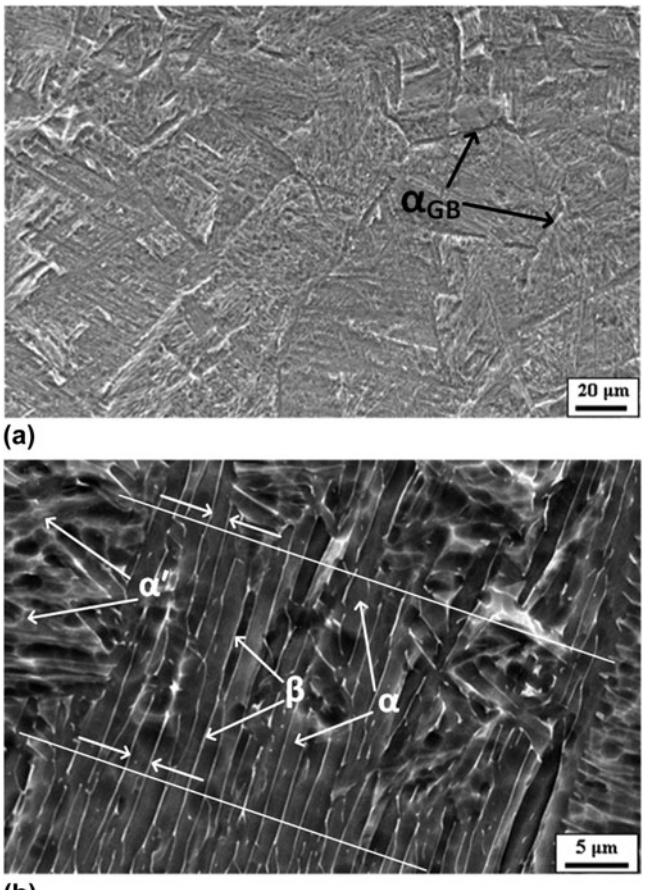


FIG. 4. Scanning electron micrographs from Z-plane of an EBAM sample: (a) 1000 × image, and (b) 5000 × image showing α-lath analysis.

https://doi.org/10.1557/jmr.2014.125 Published online by Cambridge University Press

several random lines, as shown in Fig. 3(a). From the measurements, the size of the equiaxed grains is estimated as 50.1 μm in this case (SF 36 sample).

The width of α laths was also quantitatively analyzed using SEM images, with an example shown in Fig. 4(b). The average thickness of α laths is 1.1 μm for this particular sample (SF 36).

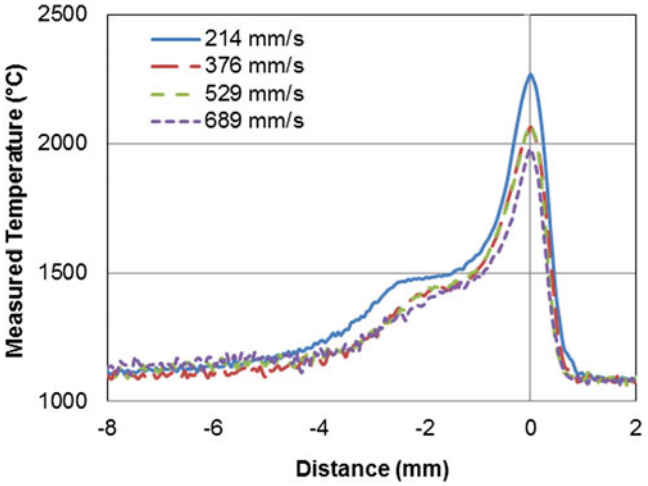


FIG. 5. Average temperature profiles from different beam speeds at build height of 24.43 mm.

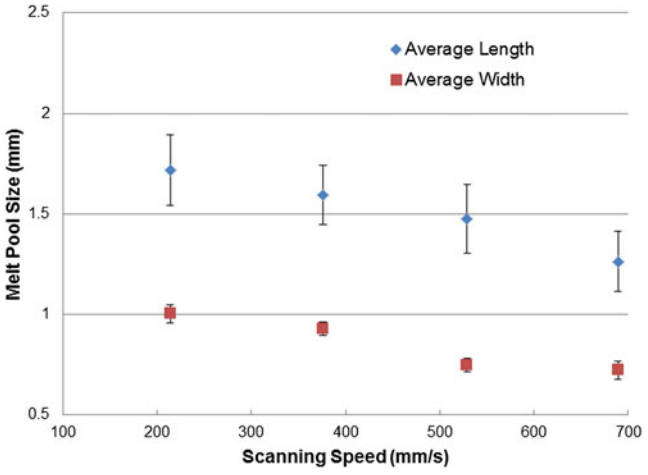


FIG. 6. Melt pool size versus beam scanning speed at build height of 24.43 mm.

B. Beam speed effects

1. Thermal characteristics

The estimated beam speed values using the method described above were 214, 376, 529, and 689 mm/s for SF 20, 36, 50, and 65, respectively. It needs to point out that the reported speed values above were at the build height of 24.43 mm, close to the end of the build. Using MATLAB software, the acquired thermal images (temperature contours) were processed to obtain temperature profiles along the beam scanning path. Multiple frames were processed and analyzed to obtain statistical data for plots. Temperature profiles from different beam speed values are shown in Fig. 5. The case of 214 mm/s (lowest speed) has the highest maximum temperatures and noticeably higher temperatures in general. On the other hand, beam speeds of 376 mm/s and 529 mm/s (SF 36 and SF 50) have close temperature distributions and 689 mm/s (SF 65) has slightly lower temperatures compared with SF 36 and SF 50. In the temperature profiles, a near-zero slope (low cooling rate) area can be identified as the liquidus–solidus transition. It also needs to point out that because of assumed Ti–6Al–4V emissivity (0.35), the transition zone is deviated from the theoretical liquidus temperature of Ti–6Al–4V (1655 °C). However, the identified liquidus temperature (T_L) is still valid for melt pool size estimates, e.g., the distance between 2 locations with T_L as the melt pool length. The average molten pool dimensions as well as standard deviations for each speed beam were calculated at the build height of 24.43 mm, shown in Fig. 6. The melt pool length and width are in the range of 1.25–1.75 mm, and 0.75–1 mm, respectively. The melt pool result also shows noticeable variations, probably because both the process and measurements are sensitive to changes in the system and environment. However, the trend clearly shows that both the molten pool length and width decrease with the increase of the beam speed, also the SF.

2. Microstructures

The influence of the beam speed to the microstructures from the X-plane specimen is shown in Fig. 7. Generally, the width of columnar structures decreases with the increase of the beam scanning speed, e.g., 109.7 μm at 214 mm/s versus 37.1 μm at 529 mm/s, shown in Table II.

TABLE II. Measured characteristic sizes from samples with various SFs.

	Columnar β size (μm)		Equiaxed β size (μm)		α-lath thickness (μm)	
Sample	Average	Standard deviation	Average	Standard deviation	Average	Standard deviation
SF 20	109.7	30.2	85.2	34.6	1.5	0.3
SF 36	41.6	6.1	50.1	16.1	1.1	0.3
SF 50	37.1	6.3	48.7	16.7	1.1	0.1
SF 65	48.6	11.6	50.8	14.5	1.0	0.3

https://doi.org/10.1557/jmr.2014.125 Published online by Cambridge University Press

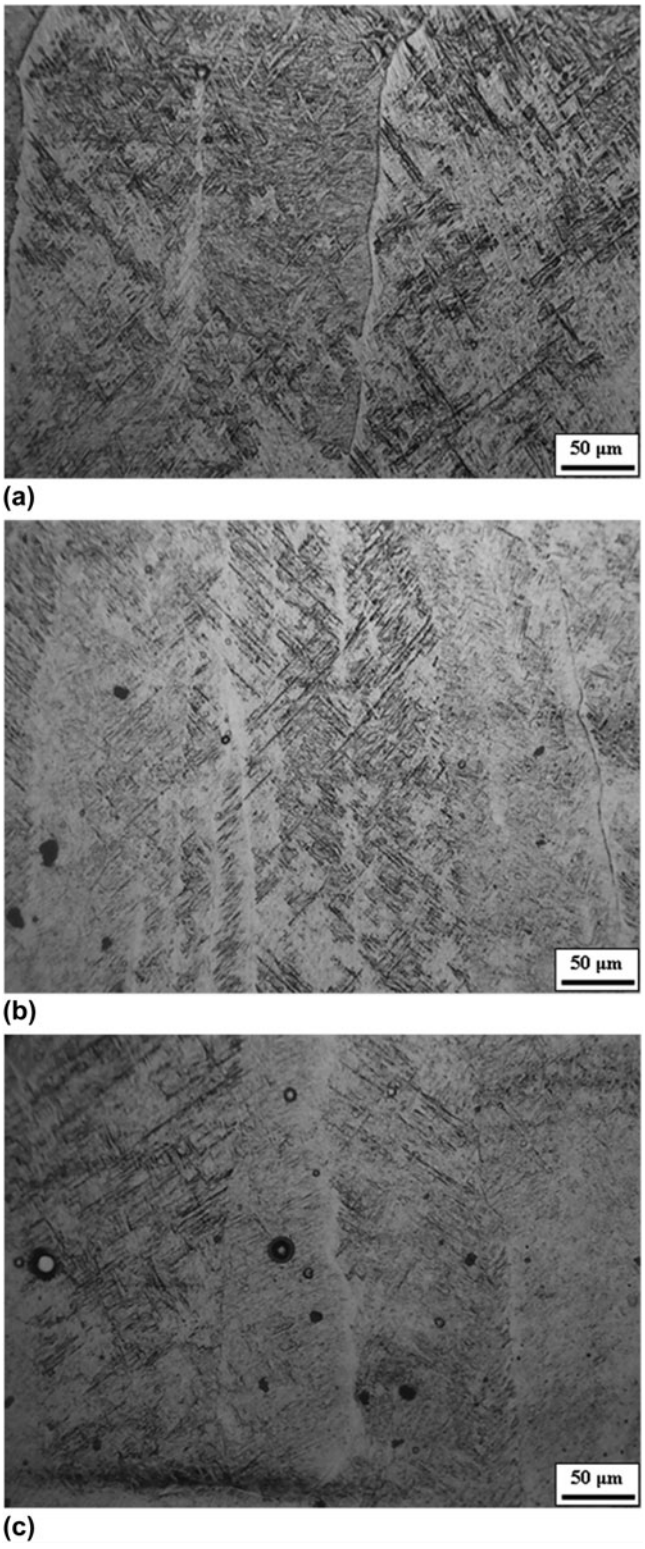


FIG. 7. OM microstructures from X-plane specimens: (a) SF 20, (b) SF 50, and (c) SF 65.

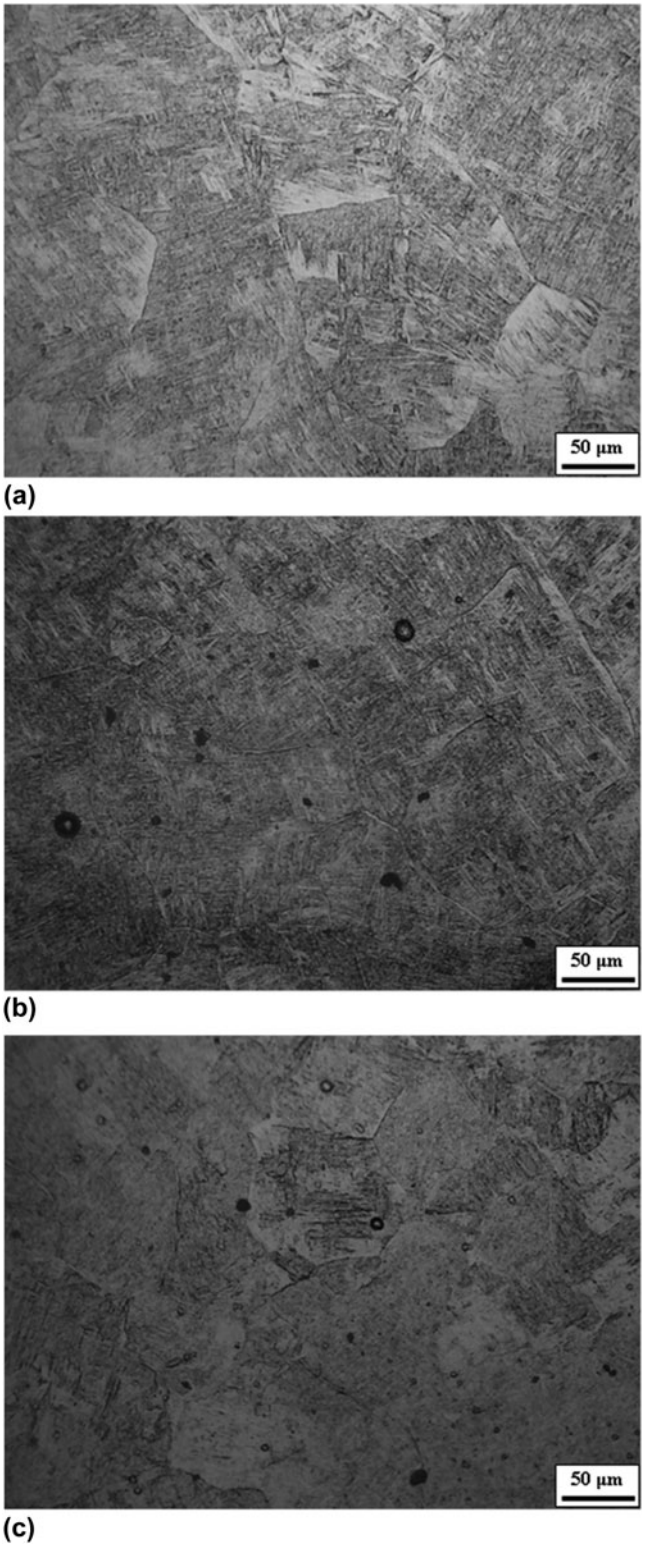


FIG. 8. OM microstructures from Z-plane specimens: (a) SF 20, (b) SF 50, and (c) SF 65.

However, the exception is the SF 65 case, in which the width of columnar structures is slightly larger than that of SF 50. For a given beam power, increasing the scanning speed would increase the cooling rate and the thermal gradient, which should result in smaller columnar β grains.[17] Gockel and Beuth[30] also reported that increasing the scanning speed will have a greater tendency to form columnar grain structures. Additionally, Wu et al.[23] also investigated the

https://doi.org/10.1557/jmr.2014.125 Published online by Cambridge University Press

beam speed effect on the grain morphology in laser AM of Ti–6Al–4V. With a higher scan speed, more nuclei can be generated due to more rapid cooling with finer grains in a long and narrow columnar morphology.

Figure 8 shows the microstructures from OM for the Z-plane specimens, which are characterized by equiaxed grains for all SF values tested. The measured sizes of equiaxed grains are also listed in Table II. The SF 20 sample (lowest beam speed, 214 mm/s) has the largest grain size of 85.2 μm, while the grain sizes of the specimens from SF 36, SF 50, and SF 65 are similar, all less than 50 μm. Gil et al.[31] studied the effects of the cooling rate on the grain size in Ti–6Al–4V and observed that the grain size is generally smaller at a faster cooling rate; however, further increasing over a certain cooling rate would not further reduce the grain size.

From this study, it is also noted that the SF 65 sample shows a larger percentage of α', as evident in SEM micrographs from the Z-plane specimens (Fig. 9). During cooling, the transformation of equiaxed β grains that exist at high temperatures produces the Widmanstätten ($\alpha + \beta$) structure. The α_{GB} is also found to form along the grain boundaries of prior β grains. Because a higher cooling rate will result in increased martensite, as expected, more α' is observed in the samples with a higher beam speed (SF 65), as shown in Fig. 9.

The microstructures from SEM micrographs (Fig. 9) exhibit the morphology of α_{GB} and primary-α colony. It was reported that the size of α-laths ranges from 0.5 to 5 μm depending on different process conditions.[9,32] The cooling rate is the key factor to control the dimension of α laths, when Ti–6Al–4V alloy is cooled down from the β-transus temperature.[17,30] The average thickness of the α-lath from different SFs is listed in Table II. The SF 20 sample has the α-lath thickness of 1.5 μm, while the α-lath thickness is about 1.0 μm for other SF cases. Murr et al.[18] reported that the thickness of the α-lath is about 1.4–2.1 μm for EBAM-made Ti–6Al–4V parts. It is evident that a higher cooling rate (associated with SF 36, 50, and 65) results in a smaller lath size. At a higher cooling rate, a greater undercooling may lead to the formation of more α nuclei and result in smaller α-laths. The experimental results, however, indicated that the α-lath size does not decrease further even with a higher cooling rate increased from a beam speed of 376 to 689 mm/s. This may be attributed to

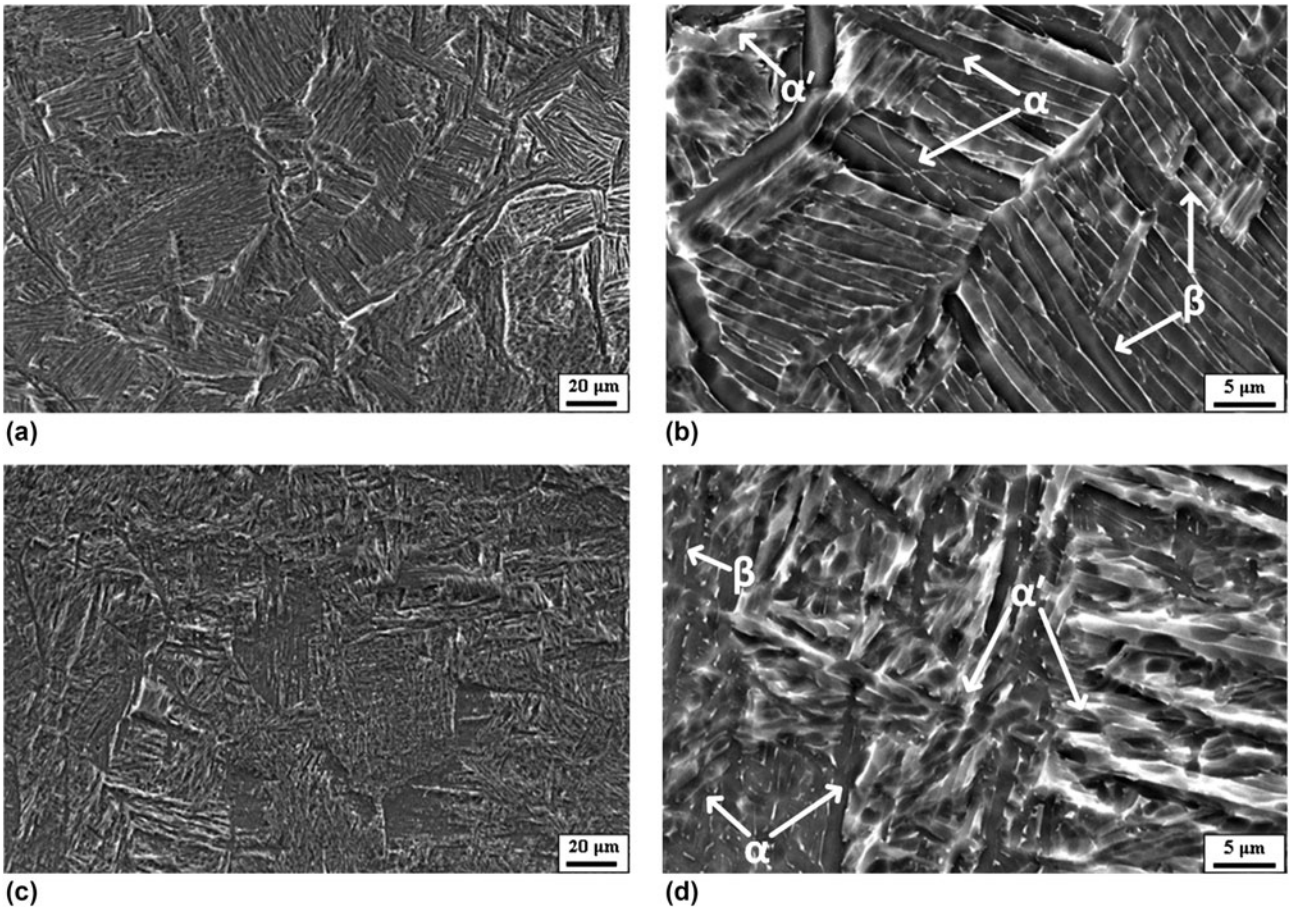


FIG. 9. SEM micrograph from Z-plane specimens: (a, b) SF 20 and (c, d) SF 50.

https://doi.org/10.1557/jmr.2014.125 Published online by Cambridge University Press

that the size of α-lath is also affected by the size of prior β grains.[33] The α phase grows in a lamellar fashion inside of β grains, so the final α-lath size is also limited by the prior β grain size. Thus, the smaller the prior β columnar structure, the finer the α-lath during the subsequent solid-state transformation. Noted from Table II, the size of prior β grains is similar between the beam speed of 376 and 689 mm/s, implying that the size of prior β grains could be a factor that influences the α-lath size, which is very close for the beam speed ranging from 376 to 689 mm/s.

IV. CONCLUSIONS

Powder-bed EBAM is one of the metal AM technologies that are capable of making full density metallic components, especially of advantage to complex geometries and/or structures. However, the EBAM process is sensitive to the process parameters, which may cause variations in build part quality. In this study, the effects of the beam scanning speed on Ti–6Al–4V microstructures from EBAM were experimentally studied. Four levels of beam scanning speeds were tested in building EBAM samples, which were subsequently used to prepare metallographic specimens for observations and analysis. During the experiment, an NIR thermal imager was also used to acquire build surface temperature distributions, which was used for the melt tool size estimate. The major findings are summarized as follows.

(i) The X-plane (side surface) specimens show columnar prior β grains with martensitic structures. The measured width of columnar grains is in the range of about 40–110 μm for the beam speeds tested in this study. With the increase of the beam scanning speed, the width of the columnar grains tends to be smaller because of a higher cooling rate during solidification.

(ii) The Z-plane (scanning surface) specimens show equiaxed grains, in the range of 50–85 μm. The grain size from the lowest-speed sample (SF 20 case) is much larger than that of samples from higher beam speed cases. The microstructure inside of equiaxed grains is Widmanstätten ($\alpha + \beta$).

(iii) In addition, increasing the scanning speed from 214 to 376 mm/s will result in finer α-laths. However, further increasing the beam speed, e.g., to 689 mm/s, will not further reduce the α-lath size.

(iv) From this study, a SF between SF 36 and SF 50 may result in fine microstructures without severe surface pores in the EBAM Ti–6Al–4V parts.

ACKNOWLEDGMENTS

This research is supported by NASA (award No. NNX11AM11A). Steven Price provided the temperature measurement results. XG also acknowledges AL EPSCoR GRSP for the financial support.

REFERENCES

1. L.E. Murr, E.V. Esquivel, S.A. Quinones, S.M. Gaytan, M.I. Lopez, E.Y. Martinez, F. Medina, D.H. Hernandez, E. Martinez, J.L. Martinez, S.W. Stafford, D.K. Brown, T. Hoppe, W. Meyers, U. Lindhe, and R.B. Wicker: Microstructures and mechanical properties of electron beam-rapid manufactured Ti-6Al-4V biomedical prototypes compared to wrought Ti-6Al-4V. *Mater. Charact.* **60**, 96 (2009).
2. X. Gong and K. Chou: Characterizations of sintered Ti-6Al-4V powders in electron beam additive manufacturing. *Proceedings of the ASME International Manufacturing Science and Engineering Conference*, L. Mears ed.; ASME, Madison, WI, 2013; p. V001T01A0022013.
3. M.F. Zäh and S. Lutzmann: Modelling and simulation of electron beam melting. *Prod. Eng.* **4**, 15 (2010).
4. N. Shen and K. Chou: Thermal modeling of electron beam additive manufacturing process: Powder sintering effect. *Proceedings of the ASME International Manufacturing Science and Engineering Conference*, S.R. Schmid, H.Y. Greenslet, and L. Mears ed.; ASME, Notre Dame, IN, 2012; p. 287.
5. X. Gong, B. Cheng, S. Price, and K. Chou: Powder-bed electron-beam-melting additive manufacturing: Powder characterization, process simulation and metrology. *Early Career Technical Conference*, P. Durbetaki and J. Donnell ed.; ASME, Birmingham, AL, 2013; p. 59.
6. S. Price, K. Cooper, and K. Chou: Evaluations of temperature measurements by near-infrared thermography in powder-based electron-beam additive manufacturing. *Proceedings of the Solid Freeform Fabrication Symposium*, D. Bourell, R.H. Crawford, C.C. Seepersad, J.J. Beaman, and H.L. Marcus ed.; University of Texas, Austin, TX, 2012; p. 761.
7. M. Koike, K. Martinez, L. Guo, G. Chahine, R. Kovacevic, and T. Okabe: Evaluation of titanium alloy fabricated using electron beam melting system for dental applications. *J. Mater. Process. Technol.* **211**, 1400 (2011).
8. A.L. Cooke and J.A. Soons: Variability in the geometric accuracy of additively manufactured test parts. *Proceedings of the Solid Freeform Fabrication Symposium*, D. Bourell ed.; University of Texas, Austin, TX, 2010; pp. 1.
9. S.S. Al-Bermani, M.L. Blackmore, W. Zhang, and I. Todd: The origin of microstructural diversity, texture, and mechanical properties in electron beam melted Ti-6Al-4V. *Metall. Mater. Trans. A* **41A**, 3422 (2010).
10. A. Safdar, L.Y. Wei, A. Snis, and Z. Lai: Evaluation of microstructural development in electron beam melted Ti-6Al-4V. *Mater. Charact.* **65**, 8 (2012).
11. A.A. Antonysamy, J. Meyer, and P.B. Prangnell: Effect of build geometry on the β-grain structure and texture in additive manufacture of Ti6Al4V by selective electron beam melting. *Mater. Charact.* **84**, 153 (2013).
12. L. Facchini, E. Magalini, P. Robotti, and A. Molinari: Microstructure and mechanical properties of Ti-6Al-4V produced by electron beam melting of pre-alloyed powders. *Rapid Prototyping J.* **15**, 171 (2009).
13. A. Christensen, R. Kircher, and A. Lippincott: Qualification of electron beam melted (EBM) Ti6Al4V-ELI for orthopaedic applications. *Proceedings of the Materials Processes for Medical Devices Conference*, J. Gilbert ed.; ASM International, Palm Desert, CA, 2007; pp. 48.
14. L.E. Murr, S.M. Gaytan, F. Medina, E. Martinez, J.L. Martinez, D.H. Hernandez, B.I. Machado, D.A. Ramirez, and R.B. Wicker: Characterization of Ti-6Al-4V open cellular foams fabricated by additive manufacturing using electron beam melting. *Mater. Sci. Eng., A* **527**, 1861–1868 (2010).
15. X. Gong, T. Anderson, and K. Chou: Review on powder-based electron beam additive manufacturing technology. In *International*

https://doi.org/10.1557/jmr.2014.125 Published online by Cambridge University Press

Symposium on Flexible Automation, M. Leu ed.; ASME, St. Louis, MO, 2012; p. 507.
16. L.E. Murr, S.M. Gaytan, F. Medina, E. Martinez, D.H. Hernandez, L. Martinez, M.I. Lopez, R.B. Wicker, and S. Collins: Effect of build parameters and build geometries on residual microstructures and mechanical properties of Ti-6Al-4V components built by electron beam melting (EBM). *Proceedings of the Solid Freeform Fabrication Symposium*, D. Bourell ed.; University of Texas, Austin, TX, 2009; p. 374.
17. S. Bontha, N.W. Klingbeil, P.A. Kobryn, and H.L. Fraser: Effects of process variables and size-scale on solidification microstructure in beam-based fabrication of bulky 3D structures. *Mater. Sci. Eng., A* **513–514**, 311 (2009).
18. L.E. Murr, S.A. Quinones, S.M. Gaytan, M.I. Lopez, A. Rodela, E.Y. Martinez, D.H. Hernandez, E. Martinez, F. Medina, and R.B. Wicker: Microstructure and mechanical behavior of Ti-6Al-4V produced by rapid-layer manufacturing, for biomedical applications. *J. Mech. Behav. Biomed. Mater.* **2**, 20 (2009).
19. M. Jamshidinia, F. Kong, and R. Kovacevic: The coupled CFD-FEM model of electron beam melting (EBM). *Proceedings of the Early Career Technical Conference (ECTC)*, P. Durbetaki and J. Donnell ed.; ASME, Birmingham, AL, 2013; p. 163.
20. T.R. Mahale: Electron beam melting of advanced materials and structures. Ph.D. Dissertation, North Carolina State University, Raleigh, NC, 2009.
21. K. Wang, W. Zeng, Y. Shao, Y. Zhao, and Y. Zhou: Quantification of microstructural features in titanium alloys based on stereology. *Rare Met. Mater. Eng.* **38**, 398 (2009).
22. S.M. Kelly: Thermal and microstructure modeling of metal deposition processes with application to Ti-6Al-4V. Ph.D. Dissertation, Virginia Polytechnic Institute and State University, Blacksburg, VA, 2004.
23. X. Wu, J. Liang, J. Mei, C. Mitchell, P.S. Goodwin, and W. Voice: Microstructures of laser-deposited Ti-6Al-4V. *Mater. Des.* **25**, 137 (2004).
24. T. Ahmed and H.J. Rack: Phase transformations during cooling in $\alpha + \beta$ titanium alloys. *Mater. Sci. Eng., A* **243**, 206 (1998).
25. J.W. Elmer, T.A. Palmer, S.S. Babu, W. Zhang, and T. Debroy: Phase transformation dynamics during welding of Ti-6Al-4V. *J. Appl. Phys.* **95**, 8327 (2004).
26. B. Baufeld, E. Brandl, and O. van der Biest: Wire based additive layer manufacturing: Comparison of microstructure and mechanical properties of Ti-6Al-4V components fabricated by laser-beam deposition and shaped metal deposition. *J. Mater. Process. Technol.* **211**, 1146 (2011).
27. W. Lu, Y. Shi, Y. Lei, and X. Li: Effect of electron beam welding on the microstructures and mechanical properties of thick TC4-DT alloy. *Mater. Des.* **34**, 509–515 (2012).
28. K. Amato, J. Hernandez, L.E. Murr, E. Martinez, S.M. Gaytan, P.W. Shindo, and S. Collins: Comparison of microstructures and properties for a Ni-base superalloy (alloy 625) fabricated by electron beam melting. *J. Mater. Sci. Res.* **1**, 3 (2012).
29. L.E. Murr, S.M. Gaytan, A. Ceylan, E. Martinez, J.L. Martinez, D.H. Hernandez, B.I. Machado, D.A. Ramirez, F. Medin, S. Collins, and R.B. Wicker: Characterization of titanium aluminide alloy components fabricated by additive manufacturing using electron beam melting. *Acta Mater.* **58**, 1887 (2010).
30. J. Gockel and J. Beuth: Understanding Ti-6Al-4V microstructure control in additive manufacturing via process maps. *Proceedings of the Solid Freeform Fabrication Symposium*, D. Bourell ed.; University of Texas, Austin, TX, 2013; p. 666.
31. F.J. Gil, M.P. Ginebra, J.M. Manero, and J.A. Planell: Formation of α-Widmanstätten structure: Effects of grain size and cooling rate on the Widmanstätten morphologies and on the mechanical properties in Ti6Al4V alloy. *J. Alloys Compd.* **329**, 142 (2001).
32. Y. Xi, M. Bermingham, G. Wang, and M. Dargusch: Finite element modeling of cutting force and chip formation during thermally assisted machining of Ti6Al4V alloy. *J. Manuf. Sci. Eng.* **135**, 061014 (2013).
33. A. Safdar: A study on electron beam melted Ti-6Al-4V. M.S. Thesis, Lund University, Lund, Sweden, 2012.

https://doi.org/10.1557/jmr.2014.125 Published online by Cambridge University Press